Sensitivity of Axisymmetric Tropical Cyclone Spinup Time to Dry Air Aloft

BRIAN H. TANG, ROSIMAR RIOS-BERRIOS, JOSHUA J. ALLAND, JEREMY D. BERMAN, AND KRISTEN L. CORBOSIERO

Department of Atmospheric and Environmental Sciences, University at Albany, State University of New York, Albany, New York

(Manuscript received 26 February 2016, in final form 26 July 2016)

ABSTRACT

The sensitivity of tropical cyclone spinup time to the initial entropy deficit of the troposphere is examined in an axisymmetric hurricane model. Larger initial entropy deficits correspond to less moisture above the initial lifting condensation level of a subcloud-layer parcel. The spinup time is quantified in terms of thresholds of integrated horizontal kinetic energy within a radius of 300 km and below a height of 1.5 km. The spinup time increases sublinearly with increasing entropy deficit, indicating the greatest sensitivity lies with initial moisture profiles closer to saturation. As the moisture profile approaches saturation, there is a large increase in the low-level, area-averaged, vertical mass flux over the spinup period because of the predominance of deep convection. Higher entropy deficit experiments have a greater amount of cumulus congestus and reduced vertical mass flux over a longer duration. Consequently, the secondary circulation takes longer to build upward, and the radial influx of angular momentum is reduced. There is also a reduction in the conversion of potential available enthalpy to horizontal kinetic energy, as a result of reduced flow down the radial pressure gradient early in the spinup period. Later in the spinup period, the low-level vortex spins up relatively quickly near the nascent radius of maximum wind in the high-entropy deficit experiments, whereas the low-level vortex spins up over a wider area in the low-entropy deficit experiments.

1. Introduction

Moisture above the boundary layer exerts a strong influence on tropical cyclone development. Gray (1979) hypothesized that high midlevel specific humidity is a necessary condition for tropical cyclogenesis. A number of studies have found that a deep tropospheric layer of near saturation precedes tropical cyclogenesis (Bister and Emanuel 1997; Raymond et al. 1998, 2011; Nolan 2007; Davis and Ahijevych 2012; Wang 2012; Komaromi 2013; Zawislak and Zipser 2014). When near saturation is achieved, deep, high precipitation efficiency convection is increasingly favored in the recirculating region of a tropical disturbance (Dunkerton et al. 2009). High precipitation efficiency convection is characterized by low rainwater evaporation rates and promotes the spinup of the low-level circulation (Raymond et al. 2007). Thus, a corollary hypothesis is that tropical disturbances with initially drier air above the boundary layer will require a greater amount of time to increase the deep tropospheric moisture and undergo tropical cyclogenesis (Emanuel 1989).

There are a number of metrics to quantify moisture around a tropical disturbance or cyclone. For example, genesis potential indices have used satellite-based water vapor brightness temperature (DeMaria et al. 2001), 600-hPa relative humidity (Camargo et al. 2007), column relative humidity (Tippett et al. 2011), and the nondimensional entropy deficit (Emanuel 2010), defined as

$$\chi = \frac{s^* - s}{s^*_{\rm SST} - s_b}, \tag{1}$$

where s, s^*, $s^*_{\rm SST}$, and s_b are the moist entropy in midlevels, the saturation moist entropy in midlevels, the saturation moist entropy at the sea surface temperature (SST), and the moist entropy of the boundary layer, respectively. The numerator is the entropy deficit Δs above the boundary layer and increases as the relative humidity decreases (Emanuel et al. 2008). The denominator is a measure of the air–sea disequilibrium.

Corresponding author address: Brian H. Tang, Department of Atmospheric and Environmental Sciences, University at Albany, State University of New York, ES 324, 1400 Washington Ave., Albany, NY 12222.
E-mail: btang@albany.edu

DOI: 10.1175/JAS-D-16-0068.1

The nondimensional entropy deficit is a strong discriminating factor in observed developing and nondeveloping tropical disturbances (Tang and Emanuel 2012b). Furthermore, the nondimensional entropy deficit has a theoretical underpinning in boundary layer quasi equilibrium (Raymond 1995) and thermodynamically connects to the convective mass flux, a key variable in the spinup of a tropical cyclone.

Emanuel (1989) derived an axisymmetric spinup time scale τ that is a vertical depth scale H, times a characteristic tropospheric density ρ_0, divided by a characteristic vertical mass flux M:

$$\tau = \frac{H\rho_0}{M}. \tag{2}$$

Understanding what controls the vertical mass flux is critical in understanding how the spinup time of tropical cyclones may vary in this framework. Almost all the upward vertical mass flux in tropical disturbances and cyclones occurs in cumulus clouds, either deep convection that reaches the tropopause or cumulus congestus that detrains at midlevels (Wang 2014). Downward mass fluxes occur in noncloudy air subsiding in between convection, at the leading edge of gravity waves induced by convective heating, or through convective downdrafts (Smith 2000).

Changing the entropy deficit above the boundary layer may have an effect on the mass flux distribution and evolution with time. Boundary layer quasi-equilibrium theory suggests that a larger entropy deficit decreases the upward convective mass flux by depressing the boundary layer entropy through convective downdrafts (Emanuel 1995) and turbulent entrainment of low-entropy air at the top of the boundary layer (Thayer-Calder and Randall 2015). Additionally, lateral entrainment of low-entropy air into convection decreases the buoyancy of an updraft and reduces the upward mass flux (Brown and Zhang 1997; James and Markowski 2010; Smith and Montgomery 2012).

Emanuel (1989) conducted three experiments with different initial nondimensional entropy deficits [(1)] in an axisymmetric model. The nondimensional entropy deficit was doubled and halved relative to a reference experiment by changing the initial moisture above the boundary layer. The onset time of intensification was correspondingly doubled and halved relative to the reference experiment, suggesting a direct relationship between the initial nondimensional entropy deficit and spinup time. Rappin et al. (2010) also found a strong correlation between the nondimensional entropy deficit and the time to maximum pressure fall in three-dimensional, cloud-resolving model experiments. However, their study varied the SST and background surface wind speed in order to vary (1) through the air–sea disequilibrium.

This study examines how dry air aloft, through the entropy deficit, affects the spinup of tropical cyclones in an axisymmetric framework. Although a direct relationship between the time of onset of intensification and the entropy deficit has been hypothesized by previous studies, the degree of nonlinearity in this relationship has not been investigated over a wide range of plausible entropy deficits. To investigate the relationship between the entropy deficit and the spinup time, we take a systematic approach using idealized initial entropy deficit profiles and an ensemble of experiments. An ensemble approach is necessary because there is an inherent stochastic component in the spinup process (Zhang and Sippel 2009). Section 2 details the methodology, section 3 examines the behavior of the experimental spinup times, section 4 compares the radial angular momentum fluxes across the experiments, section 5 compares the energetics across the experiments, section 6 examines the spinup time sensitivity to the chosen domain, and section 7 ends with conclusions.

2. Methodology

a. Axisymmetric model

The model used in this study is the Axisymmetric Simplified Pseudoadiabatic Entropy Conserving Hurricane (ASPECH) model (Tang and Emanuel 2012a, hereafter TE12), a nonhydrostatic model phrased in radius–height coordinates. The radial grid spacing is 2 km, and the vertical grid spacing is 0.3 km. The Coriolis parameter f is fixed at $5.0 \times 10^{-5}\,\mathrm{s}^{-1}$. A simple set of parameterizations is used. Radiation is parameterized through a Newtonian relaxation (Rotunno and Emanuel 1987) back to the initial temperature profile. Microphysics is parameterized using the Kessler scheme (Kessler 1969) with a constant terminal velocity for rain of $-7\,\mathrm{m\,s}^{-1}$. There are no ice-phase microphysics. Turbulence is parameterized using the methodology of Bryan and Rotunno (2009), except using the fully compressible equations. The horizontal and vertical mixing lengths in the turbulence parameterization are 1000 and 100 m, respectively. Surface fluxes are parameterized using bulk aerodynamic formulae. The enthalpy exchange coefficient is fixed at 1.2×10^{-3} (Haus et al. 2010), and the drag coefficient is 1.0×10^{-3} for 10-m wind speeds less than $5\,\mathrm{m\,s}^{-1}$ and 2.4×10^{-3} for 10-m wind speeds greater than $25\,\mathrm{m\,s}^{-1}$, varying linearly in between (Donelan et al. 2004; Black et al. 2007). Details of the dynamical core, the physics options, and numerical methods are given in TE12.

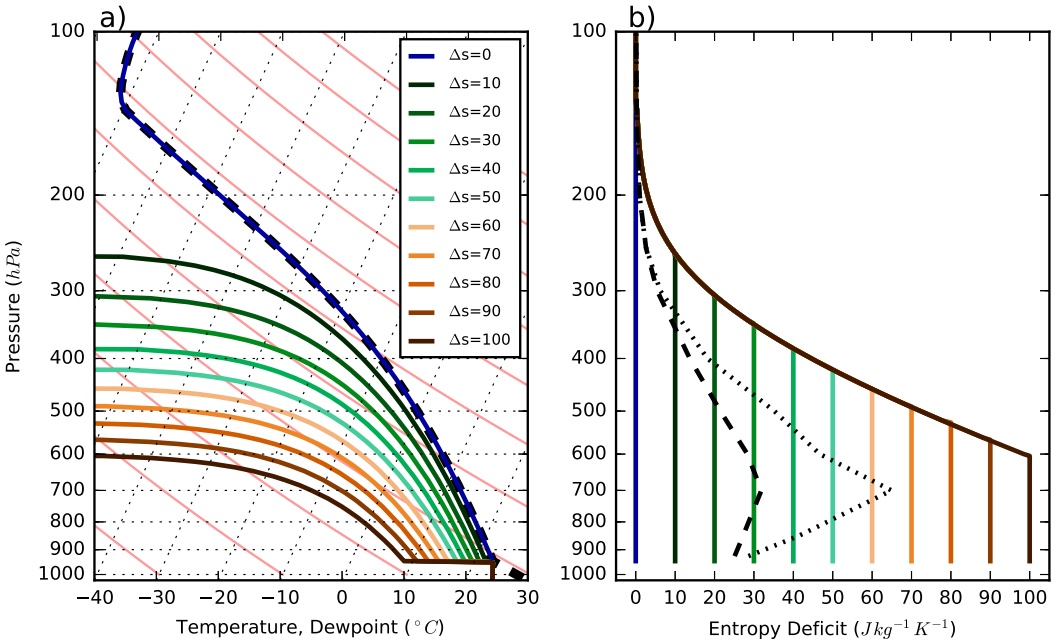

FIG. 1. (a) Initial skew T–log$p$ soundings for each experimental set. Temperature is given by the dashed black line. Dewpoint is given by the colored lines. (b) Entropy deficit profiles corresponding to the soundings in (a). The entropy deficits for the Dunion (2011) moist tropical (dashed) and Saharan air layer (dotted) reference soundings are also shown.

The treatment of thermodynamics is unique to the model and allows for a systematic experimental design. The ASPECH model uses a simplified moist entropy as its prognostic thermodynamic variable. The formulation is motivated by Bryan (2008), which simplifies the first law of thermodynamics by using a fixed, inflated value of the latent heat of vaporization L_v to compensate for neglecting the specific heat of liquid water. Additionally, the contribution from ice is not considered. Following Bolton (1980), the first law is then integrated from a reference state to saturation:

$$s = c_{\mathrm{pd}} \log\theta + \frac{L_v q}{T_L} - R_d \log p_o , \tag{3}$$

where c_{pd} is the specific heat at constant pressure of dry air, θ is the potential temperature, q is the water vapor mixing ratio, T_L is the saturation temperature, R_d is the gas constant for dry air, and p_o is the reference pressure. An empirical relationship for the saturation temperature from TE12 is substituted in order to close the system of prognostic equations in ASPECH:

$$T_L = 17.23 \log q + 362.48. \tag{4}$$

Equation (3) is optimized by selecting a value of $L_v = 2.678 \times 10^6\ \mathrm{J\,kg^{-1}}$ that minimizes the root-mean-squared error over a range of pressures, temperatures, and water vapor mixing ratios that characterize the tropical troposphere, as detailed in TE12. Note that the ASPECH model is not pseudoadiabatic per se, since it has falling precipitation, but rather the entropy of liquid water is treated as external (Raymond 2013).

The moist entropy is materially conserved in the absence of internal and boundary sources or sinks, and the moist entropy equation allows the thermodynamics of precipitating convection to be treated in a simplified manner with a slight trade-off in accuracy. The primary advantage of using a prognostic moist entropy equation is that it allows a precise specification of the initial moist entropy, which is advantageous for the experimental design, and also allows for a precise accounting of the moist entropy, which is important for the energy analysis later in the manuscript. For further details about the treatment of thermodynamics in ASPECH, see section 2a of TE12.

b. *Initial conditions*

All the experiments have the same initial temperature profile, mean subcloud-layer water vapor mixing ratio, SST, and initial vortex. The temperature profile (Fig. 1) is moist neutral relative to a subcloud-layer parcel up to the tropopause at 135 hPa. The mean subcloud-layer water vapor mixing ratio is $19\ \mathrm{g\,kg^{-1}}$, corresponding to a surface relative humidity of 75%. The SST is fixed at 30°C, 1° greater than the initial surface air temperature.

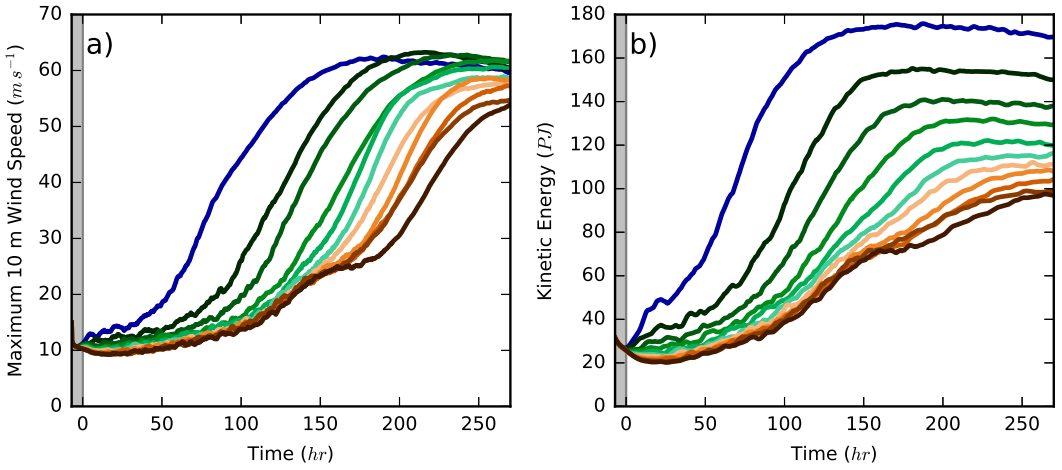

FIG. 2. Time series of the ensemble-mean (a) 10-m maximum wind speed ($m\,s^{-1}$) and (b) IHKE (PJ) for each experimental set. Colors for each set are as in Fig. 1. The gray area marks the excluded time period (see text).

The value of the air–sea temperature difference is motivated by observed values in the tropics (Fairall et al. 1996). Consequently, each experiment has the same initial air–sea disequilibrium in the denominator of (1). The initial radial structure of the vortex is specified using (6) from Knaff et al. (2011), with a radius of maximum wind of 100 km, a radius of zero wind of 500 km, and a maximum tangential wind of 15 $m\,s^{-1}$. The vortex decays with height, vanishing above 15 km. The temperature is then adjusted to be in thermal wind balance with the vortex, adapted from the procedure of Smith (2006). While the spinup depends on details of the initial vortex, it is not the focus of the current study.

The experiments are grouped into 11 sets. Each experimental set has a different mixing ratio profile above the initial lifting condensation level, corresponding to a fixed entropy deficit in the numerator of (1). The sets are incremented in 10 $J\,kg^{-1}\,K^{-1}$, ranging from saturation (Δs = 0 $J\,kg^{-1}\,K^{-1}$) to the driest profile (Δs = 100 $J\,kg^{-1}\,K^{-1}$). There is an upper bound on the entropy deficit that decreases with height, as shown in Fig. 1b, which exists because s cannot decrease below its dry value for a fixed temperature profile. For reference, the entropy deficits of the Dunion (2011) moist tropical and Saharan air layer soundings are also shown. Entropy deficits of 20–30 (30–70) $J\,kg^{-1}\,K^{-1}$ characterize a moist tropical (Saharan air layer) archetype sounding in the lower half of the troposphere.

Each experimental set has 20 ensemble members, generated by adding uniformly distributed, random perturbations to the initial water vapor mixing ratio in the lowest three model levels, similar to the methodology of Van Sang et al. (2008). The perturbations have a maximum amplitude of 1 $g\,kg^{-1}$ and a mean of zero, and they are different for each experiment. Upon integrating the experiments, the ensemble mean and spread of the spinup time within each set is evaluated. The ensemble mean filters out a portion of the stochastic component of the spinup process and allows for a cleaner evaluation of the sensitivity of the spinup time to the initial entropy deficit.

3. Spinup time

Spinup is qualitatively defined as a positive intensification trend of the low-level vortex (Nolan 2007; Nicholls and Montgomery 2013). There is a multitude of possible metrics to diagnose this process. Intensity metrics, such as point measures of the maximum wind speed or minimum sea level pressure, are one set of possibilities (Rappin et al. 2010). Figure 2a shows times series of the ensemble-mean 10-m maximum wind speed for each experimental set. The intensification can be divided into four phases: initial weakening, slow intensification, fast intensification, and quasi-steady state. This study focuses on the first two phases. Both phases are longer in duration as the initial entropy deficit increases.

Point measures of intensity, while simple and traditional, are noisy and do not capture the structure of the low-level vortex. It will become evident that structural differences between experimental sets are important, and a metric that captures these differences is advantageous. The spinup metric used in this study is the integrated horizontal kinetic energy (IHKE) over a spinup domain, extending to a radius of 300 km and a height of 1.5 km. The choice of the spinup domain is motivated by the need to choose a domain large enough to capture the

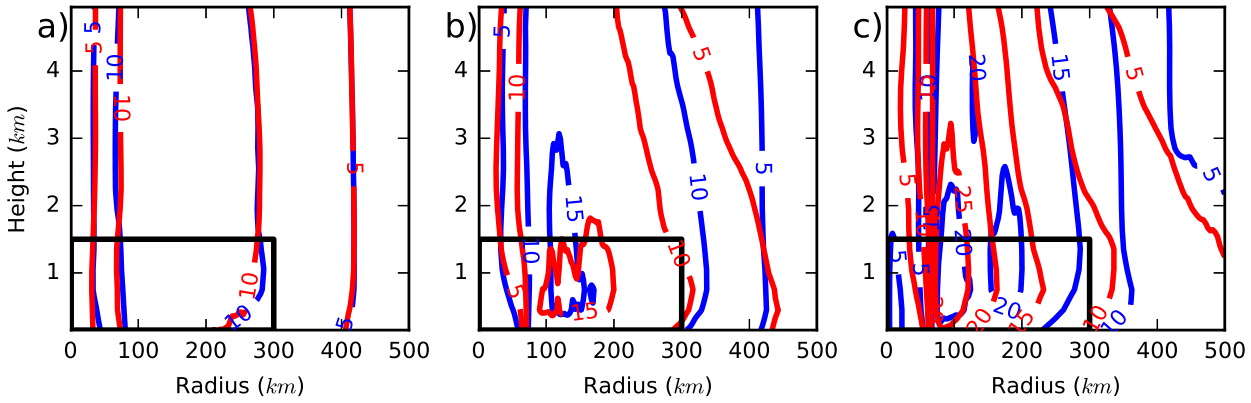

FIG. 3. Ensemble-mean tangential wind ($m\,s^{-1}$) for the $\Delta s = 0\,J\,kg^{-1}\,K^{-1}$ set (blue contours) and $\Delta s = 100\,J\,kg^{-1}\,K^{-1}$ set (red contours) at (a) t_0, (b) t_1, and (c) t_2. Contours are every $5\,m\,s^{-1}$. The black box shows the spinup domain over which the horizontal kinetic energy is integrated.

spinup of the low-level vortex, but small enough so that the IHKE is not unduly influenced by changes at very large radii. Furthermore, the radial extent of the spinup domain encompasses the convectively active region in the experiments.

Figure 2b shows time series of the IHKE for each experimental set. The same intensification phases can be qualitatively identified. However, there are differences between the 10-m maximum wind speed and the IHKE between the experimental sets. The most notable difference is the increasing separation in the IHKE with time. This separation hints that there are differences in the evolution of the structure of the low-level vortex that are not readily captured by the 10-m maximum wind speed. While there are advantages and disadvantages for any spinup metric, the IHKE is preferred for this study to capture differences in both structure and intensity between the experimental sets.

The experiments are initialized with a purely balanced vortex and no clouds. Upon integrating from such an initial condition, there exists an unrealistic adjustment period, during which a boundary layer forms, the low-level vortex weakens, and convection initiates. To avoid this adjustment period, the first 7 h of each experiment are excluded from the analysis that follows to allow time for the boundary layer to form and clouds to develop. After 7 h, the IHKE begins to noticeably diverge between the experimental sets (Fig. 2b). Henceforth, t_0 is defined to be 7 h into the model integration, and all times are relative to t_0.

We define two spinup times. First, t_1 is defined to be the final time at which the IHKE equals 1.5 times its value at t_0. Second, t_2 is defined as the final time at which the IHKE equals 2.5 times its value at t_0. Figure 3 shows the composite mean tangential wind at t_0, t_1, and t_2 for the $\Delta s = 0$ and $100\,J\,kg^{-1}\,K^{-1}$ sets. At t_0, the tangential wind fields are very similar across all the experiments, having slightly weakened below 1 km relative to initial values because of friction. By t_1, the low-level vortex has slowly intensified, and the area of tangential winds greater than $15\,m\,s^{-1}$ has appeared and expanded within the spinup domain. By t_2, the low-level vortex has continued to intensify, but structural differences in the tangential wind field become more apparent between the two experimental sets. The $\Delta s = 0\,J\,kg^{-1}\,K^{-1}$ set has a broader tangential wind field with a lower maximum value, while the $\Delta s = 100\,J\,kg^{-1}\,K^{-1}$ set has a more compact tangential wind field with a higher maximum value.

Figure 4 shows the distributions of t_1 and t_2 for each experimental set as a function of the initial entropy deficit. The mean t_1 increases from 15 to 104 h, and the mean t_2 increases from 50 to 152 h as the initial entropy deficit increases from 0 to $100\,J\,kg^{-1}\,K^{-1}$, but the relationships are sublinear. The greatest sensitivity is for entropy deficits less than $40\,J\,kg^{-1}\,K^{-1}$. As the initial entropy deficit exceeds $50\,J\,kg^{-1}\,K^{-1}$, the spinup time still generally increases, albeit at a slower rate. The difference between t_2 and t_1 increases from a mean of 35 to 48 h as the initial entropy deficit increases from 0 to $100\,J\,kg^{-1}\,K^{-1}$. There is much less variation in the difference between t_2 and t_1 as a function of the initial entropy deficit compared to variations in t_1, suggesting that differences in spinup time are largely controlled by processes occurring before t_1.

There are 2 degrees of freedom in setting the initial entropy deficit profiles. The first is the magnitude of the entropy deficit, and the second is the depth of the constant entropy deficit layer, which decreases with increasing entropy deficit (Fig. 1b). To investigate how much the depth is responsible for the nonlinearity, we repeated the experiments with a saturated layer above

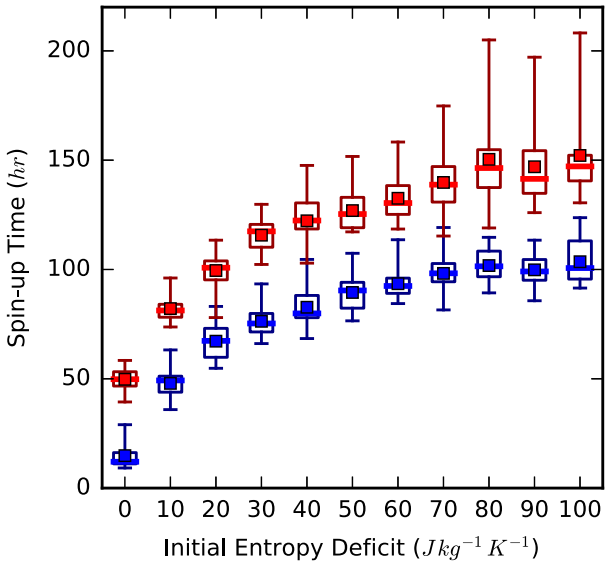

FIG. 4. Box plots of spinup time, t_1 (blue) and t_2 (red), as a function of the initial entropy deficit. The box extends from the lower to upper quartile, the line through the box gives the median, the square gives the mean, and the whiskers show the range.

600 hPa such that the entropy deficit is only realized in a fixed layer from the initial lifting condensation level to 600 hPa. The result is a small (5–10 h) downward shift in t_1 and t_2, except for the initially saturated case (not shown), but the sublinear relationship remains, and the results that follow do not appreciably change. Hence, most of the sensitivity appears to be due to the magnitude of the entropy deficit itself.

The ensemble range in t_1 and t_2 gives a measure of the stochastic effects of convection on spinup. There is substantial spread in the spinup time for all the experimental sets, which highlights the necessity of using an ensemble framework (Fig. 4). A larger initial entropy deficit tends to increase the uncertainty in t_2. For example, the range in t_2 for the $\Delta s \geq 80\,\mathrm{J\,kg^{-1}\,K^{-1}}$ sets is 70–90 h.

The entropy deficit in each experiment evolves from the initial state. Figure 5 shows the ensemble-mean entropy deficit field at $0.25t_1$, t_1, and t_2 for the $\Delta s = 0, 20, 50$, and $100\,\mathrm{J\,kg^{-1}\,K^{-1}}$ sets. At $0.25t_1$, convection occurs within a radius of 300 km in all the sets. As Δs increases, the convection transitions from a deep regime to a congestus regime (Figs. 5a–d). Wang (2014) noted the role of cumulus congestus, including shallow convection, in moistening the middle troposphere during tropical cyclogenesis. The convective moistening is made evident by the smaller entropy deficits where convection is active.

Convection takes longer to decrease the entropy deficit where the entropy deficit is initially larger. At t_1, all the simulations show entropy deficits less than $20\,\mathrm{J\,kg^{-1}\,K^{-1}}$ between a radius of 75 and 200 km over a deep column (Figs. 5e–h) and the presence of deep convection. At t_2, entropy deficits less than $10\,\mathrm{J\,kg^{-1}\,K^{-1}}$ exist in a deep column around a radius of 100 km, where the deep convection has organized into a more coherent feature (Figs. 5i–l). The intensification of the vortex and inward contraction of the radius of maximum wind is tied to this coherent, deep convection (Figs. 3b,c). Additionally, the width of the convecting region is narrower for the experiments with larger initial entropy deficits. Adjacent to the low-entropy deficit column, compensating subsidence causes the relative humidity to decrease and the entropy deficit to rise. High-entropy deficit air ($>50\,\mathrm{J\,kg^{-1}\,K^{-1}}$) subsides all the way to the surface outward of 300 km in the $\Delta s = 100\,\mathrm{J\,kg^{-1}\,K^{-1}}$ set (Figs. 5d,h,l).

There is a distribution of shallow to deep convection across the experiments with differing vertical mass flux profiles. Figures 6a and 6b show contoured frequency by altitude diagrams (CFADs) of the convective mass flux for the $\Delta s = 0$ and $100\,\mathrm{J\,kg^{-1}\,K^{-1}}$ sets. The CFADs are constructed by stacking normalized histograms of the vertical mass flux, which includes dry air, water vapor, and cloud water, at each model level for points where the liquid water mixing ratio exceeds $0.01\,\mathrm{g\,kg^{-1}}$ for the period through t_2. For the $\Delta s = 0\,\mathrm{J\,kg^{-1}\,K^{-1}}$ set, the CFAD for positive mass fluxes flares outward with height from 5 to 11 km, where the CFAD has its maximum positive skewness. In contrast, the CFAD for the $\Delta s = 100\,\mathrm{J\,kg^{-1}\,K^{-1}}$ set has more of an hourglass shape, with relatively large positive skewness between 2 and 4 km, and between 10 and 12 km.

Figure 6c shows the sign of the difference between the $\Delta s = 0$ and $100\,\mathrm{J\,kg^{-1}\,K^{-1}}$ CFADs. In the upper troposphere, the $\Delta s = 0\,\mathrm{J\,kg^{-1}\,K^{-1}}$ set has a higher frequency of nonzero convective mass flux, except for the most extreme positive values, compared to the $\Delta s = 100\,\mathrm{J\,kg^{-1}\,K^{-1}}$ set. The higher frequency is the result of deep convective plumes rising and entraining moist air through a deep column and the convectively forced descent in between. The $\Delta s = 100\,\mathrm{J\,kg^{-1}\,K^{-1}}$ set has a higher frequency of upward mass fluxes greater than $3.5\,\mathrm{kg\,s^{-1}\,m^{-2}}$ associated with strong, deep convective updrafts. However, these strong updrafts take longer to appear and are confined to a more narrow region compared to the $\Delta s = 0\,\mathrm{J\,kg^{-1}\,K^{-1}}$ set (Fig. 5l). Additionally, the $\Delta s = 100\,\mathrm{J\,kg^{-1}\,K^{-1}}$ set has a greater frequency of positive convective mass fluxes below 3 km, resulting from a greater percentage of cumulus congestus with bottom-heavy mass flux profiles during spinup (Fig. 5d) (Wang 2014). The $\Delta s = 0\,\mathrm{J\,kg^{-1}\,K^{-1}}$ set has stronger, albeit rare, convective downdrafts less

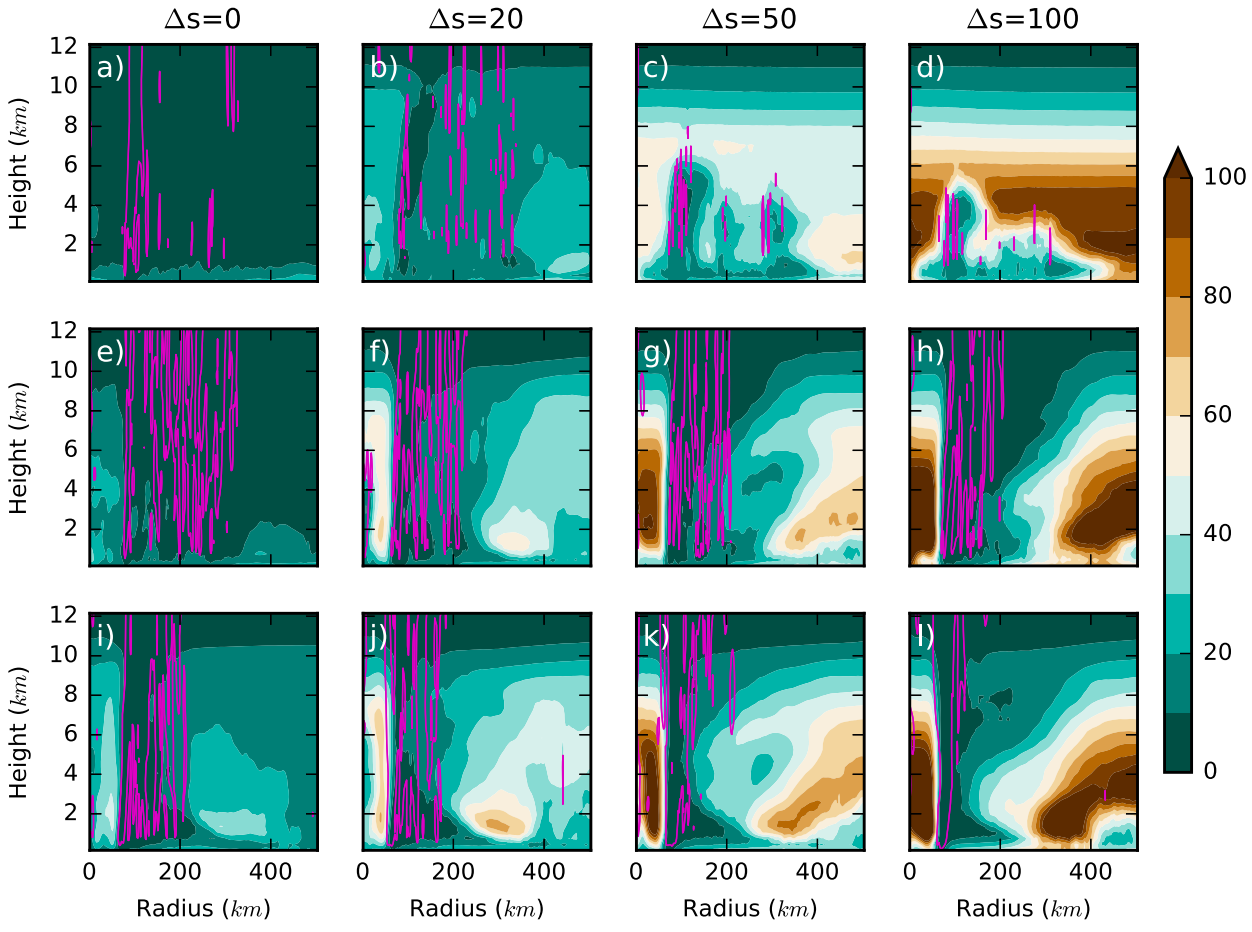

FIG. 5. Ensemble-mean entropy deficits (shading; J kg^{-1} K^{-1}) for (left–right) initial Δs = 0, 20, 50, and 100 J kg^{-1} K^{-1} at (a)–(d) 0.25t_1, (e)–(h) t_1, and (i)–(l) t_2. Magenta contours indicate where the ensemble-mean vertical velocity exceeds 0.1 m s^{-1}.

than -2 kg s^{-1} m^{-2}, whereas these are absent in the Δs = 100 J kg^{-1} K^{-1} set—a result that is also present in the CFADs of the mass flux, including noncloudy air (not shown). These findings are consistent with those of James and Markowski (2010), who found that dry air aloft did not produce stronger convective downdrafts in high-resolution simulations of continental convection. The CFADs do suggest that the dry air does increase the relative frequency of convective downdrafts between -2 and -0.5 kg s^{-1} m^{-2} in the lower troposphere.

Figure 7 shows ensemble-mean vertical mass flux profiles averaged in the innermost 300 km through the two spinup time periods. The vertical mass flux tends to decrease with increasing initial entropy deficit, with the largest decrease between 0 and 30 J kg^{-1} K^{-1}. Bottom-heavy mass flux profiles characterize convection in the period before t_1 (Fig. 7a). The maximum vertical mass flux shifts to lower values and heights as the initial entropy deficit increases. Differences in the vertical mass flux profiles are even greater when averaged over the period through t_2 (Fig. 7b). The experiments with initial entropy deficits of 0 and 10 J kg^{-1} K^{-1} are characterized by top-heavy mass flux profiles, associated with the presence of deep convection with radial inflow over a deep, tropospheric layer. For larger initial entropy deficits, the mass flux increases in the middle and upper troposphere with time, but over a smaller annulus (Fig. 5). The increase in mass flux also occurs more slowly because t_1 is longer for larger initial entropy deficits.

The initial entropy deficit clearly affects the evolution of the vertical mass flux profile. The vertical mass flux is hypothesized to be an important variable controlling the spinup time from the Emanuel (1989) scaling. To test this hypothesis, the observed model spinup times, t_1 and t_2, are compared with the theoretical spinup time scale given by (2). Since spinup concerns the low-level vortex, and to remain consistent with the spinup domain, the vertical mass flux is spatially averaged over the innermost 300 km and lowest 1.5 km for each experiment. The spatially averaged vertical mass flux is also averaged

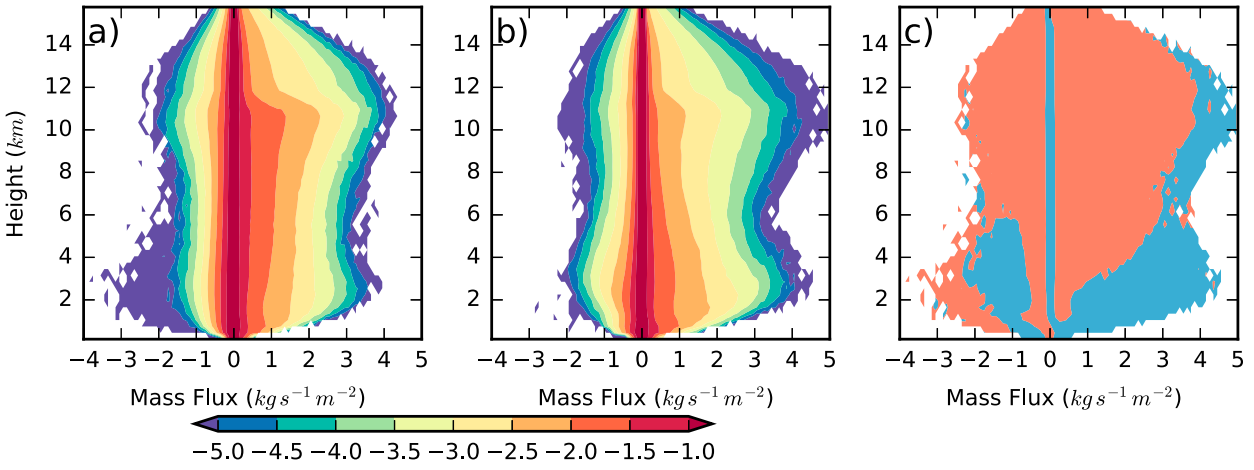

FIG. 6. CFADs of the convective mass flux for the (a) $\Delta s = 0$ and (b) $\Delta s = 100\,\mathrm{J\,kg^{-1}\,K^{-1}}$ sets for the period through t_2. Note the scale is logarithmic (base 10) in order to resolve the tails of the CFADs. (c) Sign of the difference between (a) and (b), where the red shading represents points where the CFAD is larger for (a), and the blue shading represents points where the CFAD is larger for (b).

through t_1 and t_2, which is then used in the denominator of (2) to calculate τ_1 and τ_2, respectively. For the numerator, the vertical depth scale is set at 15 km, the initial height of the tropopause, and the characteristic tropospheric density is set at $0.6\,\mathrm{kg\,m^{-3}}$, the initial vertical average through 15 km.

Figure 8 shows a comparison of the experimental model spinup times and theoretical spinup time scales. Both the spinup times and the time scales are shifted by their ensemble means of the $\Delta s = 0\,\mathrm{J\,kg^{-1}\,K^{-1}}$ set to facilitate comparison. The mean spinup times have a scaling near to that of theoretical expectations, as indicated by the means approximately aligned along the one-to-one line. The means filter out part of the stochastic component. The mean experimental spinup time tends to be slightly faster than the theoretical spinup time overall, which may be caused by uncertainty in the characteristic parameters in the numerator of (2) or boundary layer processes that the theory simplifies (Smith et al. 2009). There is large variance in τ_1, especially for the lower initial entropy deficit experiments. Small absolute differences in the vertical mass flux, due to differences in convection between the experiments, can lead to large differences in τ, especially for short averaging periods. The sublinear relationship between the initial entropy deficit and the spinup time is also apparent, as given by the increasing overlap between different ensemble sets for increasing Δs, especially for $\Delta s > 40\,\mathrm{J\,kg^{-1}\,K^{-1}}$. This pattern is consistent with the separation in the ensemble-mean vertical mass flux profiles, which is small for $\Delta s > 40\,\mathrm{J\,kg^{-1}\,K^{-1}}$ (Fig. 7).

The mean vertical mass flux profiles are linked to the structure of the mean radial mass flux. Through t_1 at a radius of 300 km, negative radial mass fluxes, signifying inflow, are larger in magnitude and occur over a deeper layer as the initial entropy deficit decreases (Fig. 9a). On the other hand, as the initial entropy deficit increases above $40\,\mathrm{J\,kg^{-1}\,K^{-1}}$, there exists weak radial outflow above 1.5 km. The radial mass flux profiles correspond well to what is expected from Fig. 7a and conservation of mass. Moving inward to a radius of 100 km, the radial mass fluxes below 1 km are not as large as the fluxes at 300 km but still show a trend toward more negative values as the initial entropy deficit decreases.

Through t_2, the radial mass flux profiles are similar in shape, albeit shifted to the left toward stronger inflow (Fig. 9b). There is reduced separation between the radial mass fluxes at 100 and 300 km for the high-entropy deficit sets. Furthermore, the $\Delta s = 100\,\mathrm{J\,kg^{-1}\,K^{-1}}$ set has the strongest inflow at 100 km through t_2, whereas this set had one of the weakest inflow profiles through t_1.

Details of the changes in radial inflow structure are associated with changes in the structure and intensity of the low-level vortex in each experimental set. To better understand how the initial entropy deficit affects spinup of the low-level vortex, it is not the radial mass flux, per se, but the radial flux of angular momentum and energy that gives further insights into spinup from complementary dynamical and energetic viewpoints.

4. Angular momentum

Radial inflow transports higher-angular-momentum air inward and accelerates the tangential wind within the boundary layer if the angular momentum flux convergence exceeds frictional torques (Smith et al. 2009). Figure 10 shows the evolution of the ensemble-mean angular momentum flux at a radius of 300 km for four of

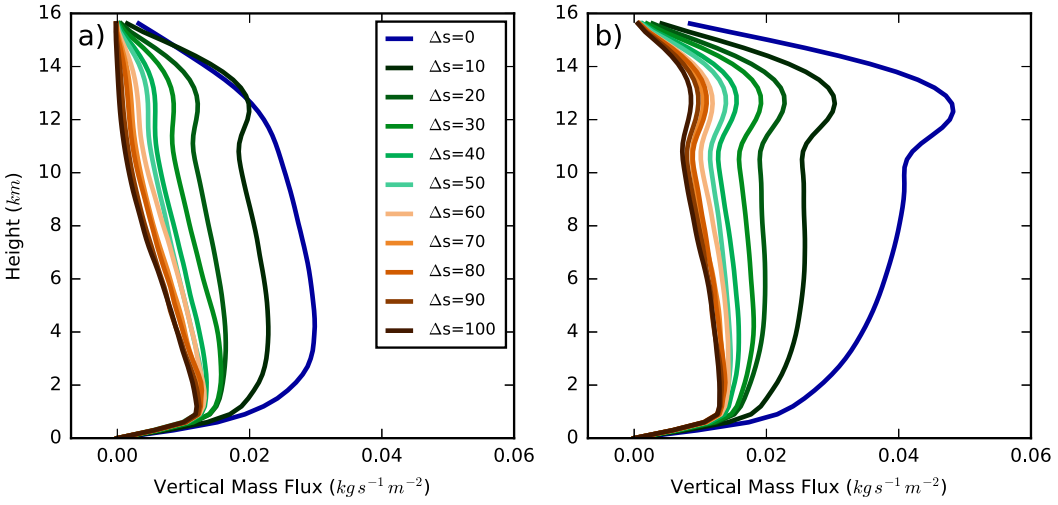

FIG. 7. Ensemble-mean vertical mass flux profiles averaged in the innermost 300 km through (a) t_1 and (b) t_2.

the experimental sets. Since the angular momentum is a positive definite quantity, the sign of the angular momentum flux is strictly determined by the sign of the radial wind at this radius. Consistent with the formation of deep convection, a secondary circulation spanning the full troposphere develops between t_0 and t_1. As the initial entropy deficit increases, the formation of a troposphere-deep secondary circulation is delayed. The secondary circulation takes time to build upward, as indicated by the strip of positive angular momentum fluxes originating at 1.5 km in height that moves to the upper troposphere as time progresses (Figs. 10b–d). This pattern is consistent with the experimental sets that have mean radial outflow above 1.5 km over the period before t_1 (Fig. 9a).

However, even after t_1 and the establishment of deep convection, the angular momentum fluxes do not converge toward the same pattern in the experimental sets. The $\Delta s = 0\,\mathrm{J\,kg^{-1}\,K^{-1}}$ set has the most robust secondary circulation through t_2 and beyond, resulting in the deepest and most negative low-level radial fluxes of angular momentum at 300 km (Fig. 10a). As the initial entropy deficit increases, the inward flux of angular momentum remains shallower and weaker. These patterns are consistent with the radial mass flux profiles in Fig. 9.

Differences in the radial flux of angular momentum affect the structural evolution of the low-level vortex, as seen in Fig. 11, which shows the ensemble average, radial angular momentum flux convergence at the lowest model level. Before t_1, the radial angular momentum

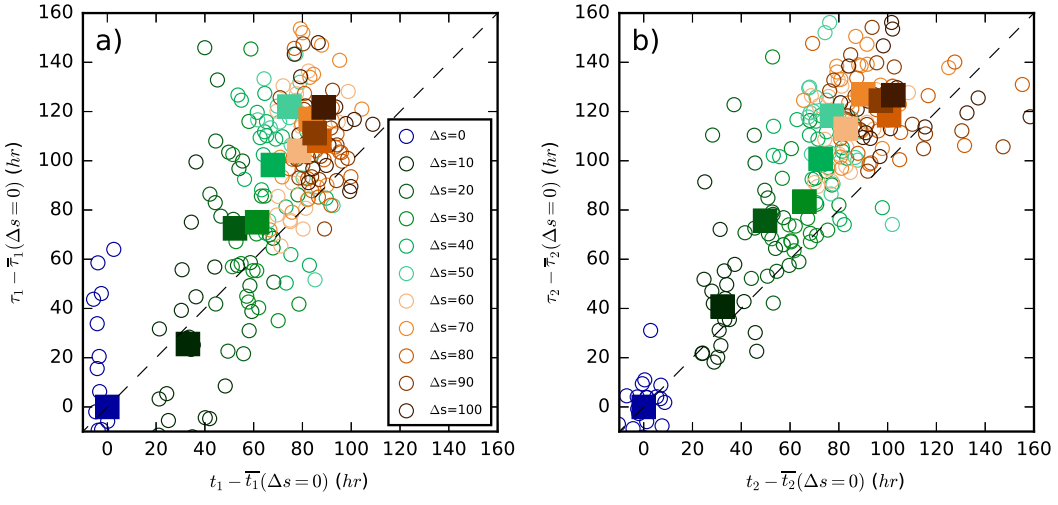

FIG. 8. Experimental spinup times vs the theoretical spinup time scales, given by (a) t_1 and τ_1 and (b) t_2 and τ_2. The circles are individual ensemble members, and the filled squares are ensemble means. The dashed line is the one-to-one line. The times are shifted by the mean values for the $\Delta s = 0\,\mathrm{J\,kg^{-1}\,K^{-1}}$ set.

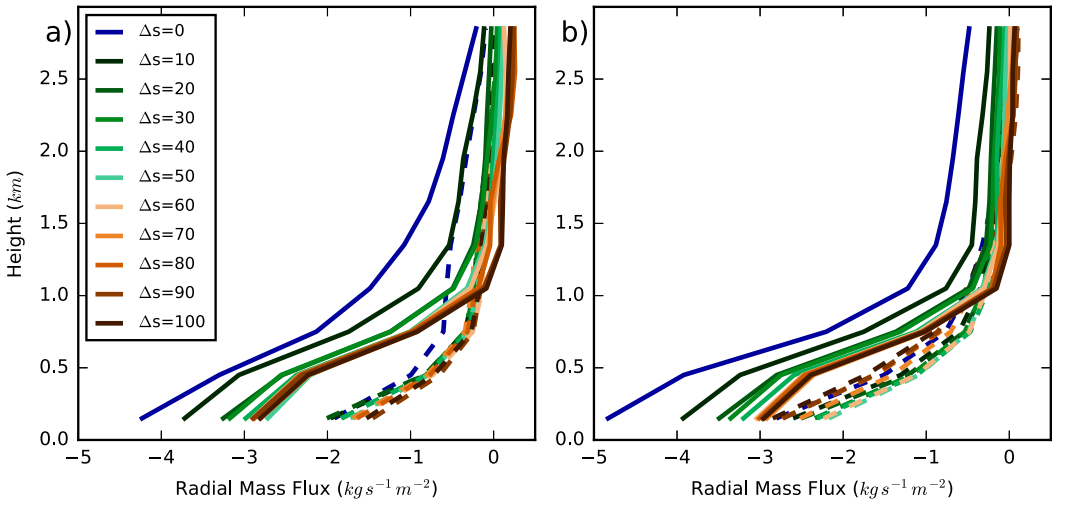

FIG. 9. Ensemble-mean radial mass flux profiles at 300 (solid) and 100 km (dashed) averaged through (a) t_1 and (b) t_2.

flux convergence profile is mostly flat for radii greater than 75 km and does not show any clear dependence on the initial entropy deficit. Recall that t_1 represents a much longer period of time for larger initial entropy deficits, so weak angular momentum flux convergence persists for about 100 h in the $\Delta s = 100\,\mathrm{J\,kg^{-1}\,K^{-1}}$ set and only about 15 h in the $\Delta s = 0\,\mathrm{J\,kg^{-1}\,K^{-1}}$ set.

Between t_1 and t_2, greater differences emerge between the experimental sets. While all the experiments generally have an increase in the magnitude of the radial angular momentum flux convergence, the experiments with a larger initial entropy deficit have strongly peaked profiles, with maxima around 75 km (Fig. 11b). The peaks are tied to more radially confined annuli of convection, as seen in Figs. 5i–l at t_2. The confinement of convection to a small annulus results in a sharply peaked heating profile near the radius of maximum wind. Such a heating profile induces a strong low-level radial inflow response, as seen at 100 km in Fig. 9 in the larger initial entropy deficit experiments. Inward of 100 km, there then exists a correspondingly peaked radial angular momentum flux convergence profile, quickly spinning up the tangential winds around this peak (Shapiro and Willoughby 1982).

A broader convective envelope extending well away from the radius of maximum wind, as is found in the

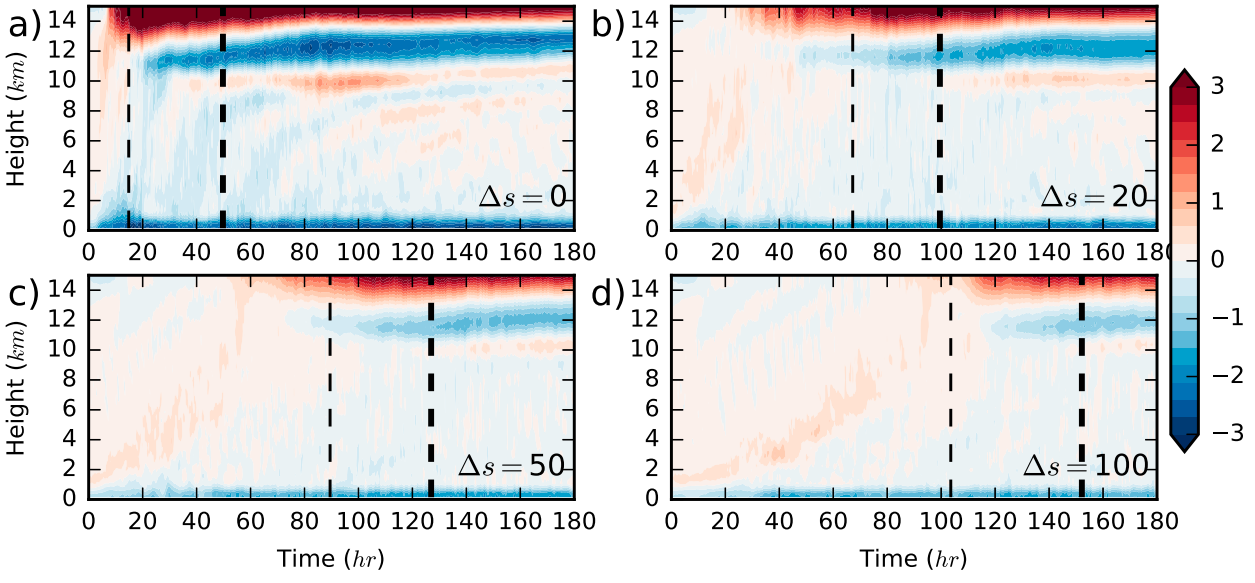

FIG. 10. Time–height plot of the ensemble-mean radial angular momentum flux ($10^7\,\mathrm{m^3\,s^{-2}}$) at a radius of 300 km for the (a) $\Delta s = 0$, (b) $\Delta s = 20$, (c) $\Delta s = 50$, and (d) $\Delta s = 100\,\mathrm{J\,kg^{-1}\,K^{-1}}$ sets. Blue (red) shading signifies radial import (export). The thin dashed line is the ensemble-mean t_1, and the thick dashed line is the ensemble-mean t_2.

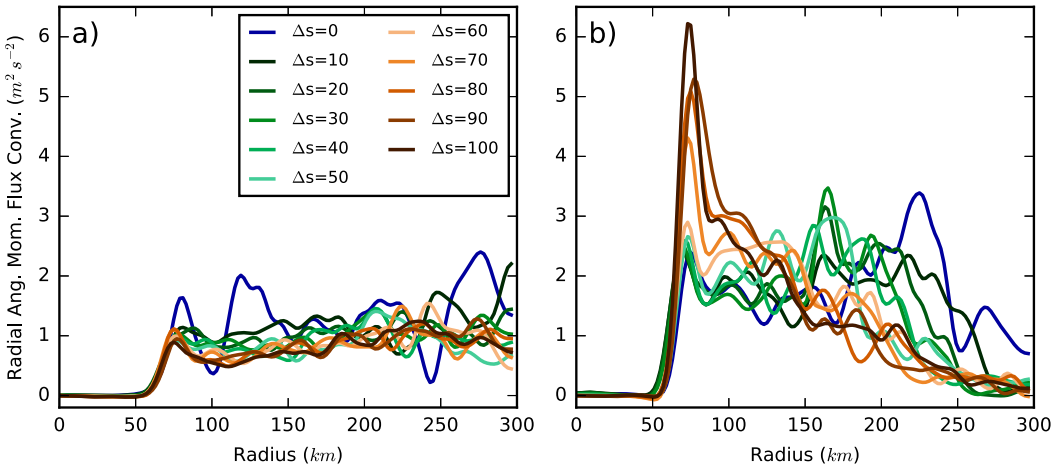

FIG. 11. Ensemble-mean angular momentum flux convergence (10^{-5} m^2 s^{-2}) at the lowest model level averaged over (a) the period through t_1 and (b) from t_1 to t_2. The radial profiles have been smoothed using a 1–2–1 filter 10 times.

lower initial entropy deficit experiments at t_2, tends to maintain a flatter angular momentum flux convergence profile. Such a profile spins up the vortex more broadly (Vigh and Schubert 2009; Musgrave et al. 2012; Rogers et al. 2013). Hill and Lackmann (2009), Wang (2009), and Ying and Zhang (2012) also presented evidence that the size of a tropical cyclone wind field is affected by the convective heating in rainbands and the associated diabatic generation of potential vorticity. The development of rainbands, and thus the evolution of the radial profile of the tangential wind, is hypothesized to be sensitive to the environmental moisture.

In summary, the larger initial entropy deficit experiments tend to have a more compact vortex and less IHKE. Conversely, experiments with smaller initial entropy deficit tend to have a broader vortex and more IHKE. The results of this study indicate that not only is the spinup time sensitive to the environmental moisture, but the development of the kinematic structure is as well.

5. Energetics

a. Kinetic energy

Since the spinup metric is the IHKE, sources and sinks of horizontal kinetic energy over the specified spinup domain in the ASPECH model are now examined. The radial and tangential momentum equations in ASPECH are

$$\frac{du}{dt} = fv + \frac{v^2}{r} - c_{\mathrm{pd}}\theta_\rho \frac{\partial \pi}{\partial r} + D_u, \quad \text{and} \tag{5}$$

$$\frac{dv}{dt} = -fu - \frac{uv}{r} + D_v, \tag{6}$$

where u is the radial wind, v is the tangential wind, f is the Coriolis parameter, r is radius, c_{pd} is the specific heat of dry air at constant pressure, θ_ρ is the density potential temperature, π is the Exner function, and (D_u, D_v) are the turbulent mixing terms.

The horizontal kinetic energy, $k_h = 0.5(u^2 + v^2)$, equation is

$$\frac{dk_h}{dt} = -c_{\mathrm{pd}}\theta_\rho u \frac{\partial \pi}{\partial r} + uD_u + vD_v. \tag{7}$$

The first term on the rhs of (7) is the conversion of potential available enthalpy (defined in the next section) to kinetic energy, and the remaining terms are sinks due to turbulence and friction.

Defining $K_h = \rho_d k_h$, using conservation of mass, and integrating over the spinup domain yields an integrated form of the kinetic energy equation:

$$\frac{\partial}{\partial t}\int_V K_h = -\int_S \mathbf{u} K_h \cdot \mathbf{n} - \int_V c_{\mathrm{pd}}\rho_d\theta_\rho u \frac{\partial \pi}{\partial r} + \int_V \rho_d (uD_u + vD_v), \tag{8}$$

where $\mathbf{u} = (u, w)$, w is the vertical wind, ρ_d is the dry density, V represents an integral over the cylindrical spinup domain, and S represents a surface integral of the cylinder with normal unit vector $\mathbf{n}$.

Figure 12 depicts an energy diagram for ASPECH. The horizontal kinetic energy budget comprises the right side of the diagram. The box represents the lhs of (8), and the arrows represent the rhs of (8). The directions of the arrows are chosen to reflect the generation, dissipation, fluxes, or conversions of energy in this study for the chosen spinup domain. The only way to

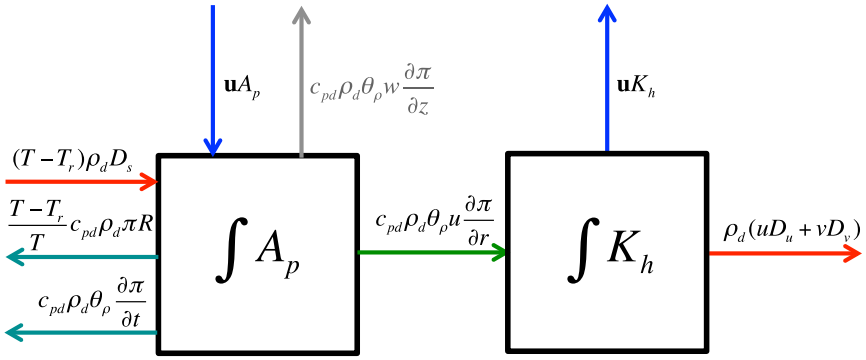

FIG. 12. Energy diagram for the integrated potential available enthalpy and horizontal kinetic energy in the spinup domain. Boxes show reservoirs of each quantity in the spinup domain. Arrows are sources and sinks of each quantity (see text). Colors of the arrows correspond to colors of the bars in Figs. 13 and 15.

increase the horizontal kinetic energy is for there to be conversion of energy as a result of flow down a radial pressure gradient. Net advective fluxes tend to export horizontal kinetic energy to higher levels as the vortex grows in depth during spinup, and friction removes kinetic energy. Hence, the structure of the radial inflow of the developing secondary circulation is paramount to the spinup evolution of a tropical cyclone.

Figure 13a shows that there is a reduction in the conversion rate of potential available enthalpy to kinetic energy as the initial entropy deficit increases, from an ensemble mean of 1.2 TW for the $\Delta s = 0\,\mathrm{J\,kg^{-1}\,K^{-1}}$ set to 0.6 TW for the $\Delta s = 100\,\mathrm{J\,kg^{-1}\,K^{-1}}$ set. Variations in both the advective flux and frictional components as a function of the initial entropy deficit are smaller, so the net surfeit of power to spin up the vortex (white bars) decreases rapidly as the initial entropy deficit increases from 0 to $20\,\mathrm{J\,kg^{-1}\,K^{-1}}$ and decreases more slowly for larger initial entropy deficits.

A reduction in the conversion rate of potential available enthalpy to kinetic energy must imply there is less flow down the radial pressure gradient over the spinup domain as a whole. Figures 14a–d show the $\Delta s = 0\,\mathrm{J\,kg^{-1}\,K^{-1}}$ set has the strongest and deepest radial flow down the pressure gradient in the spinup domain. As the initial entropy deficit increases, the radial flow down the pressure gradient becomes shallower and weakens. However, there is little difference between the $\Delta s = 50$ and $100\,\mathrm{J\,kg^{-1}\,K^{-1}}$ sets, consistent with the similar conversion rates between the two sets in Fig. 13a.

Between t_1 and t_2, the rate of change of the horizontal kinetic energy is similar across all experiments (Fig. 13b). The similar rates are consistent with less variation in the difference between t_2 and t_1 as a function of the initial entropy deficit compared to variations in t_1 (Fig. 4). Each component of the horizontal kinetic energy budget has increased in magnitude from t_1 to t_2. In particular, increases in the conversion term are generally larger with increasing initial entropy deficit.

Despite the similar rates of change of horizontal kinetic energy over this period, the spatial distribution of this change within the spinup domain differs across the experimental sets. Figures 14e–h shows radial velocities less than $-4\,\mathrm{m\,s^{-1}}$ overlapping radial gradients in pressure of 3–5 hPa per 100 km. The area in the spinup domain where the product of these two variables is maximized in magnitude shifts inward with increasing initial entropy deficit, from 200–300 km in the $\Delta s = 0\,\mathrm{J\,kg^{-1}\,K^{-1}}$ set to 100–200 km in the $\Delta s = 100\,\mathrm{J\,kg^{-1}\,K^{-1}}$ set. Thus, there is greater conversion of potential available enthalpy to kinetic energy at smaller radii as the initial entropy deficit increases. The result is a more compact low-level vortex.

b. *Potential available enthalpy*

Marquet (1991, 1993) defined an available enthalpy or exergy as the amount of work obtainable as parcels reach an equilibrium reference state. The available enthalpy is similar conceptually to available potential energy (Lorenz 1955, 1978) and available energy (Bannon 2004, 2005). One of the main advantages of available enthalpy is that it may be applied to limited domains and, when paired with the thermodynamics of ASPECH, yields a simple framework for a comprehensive investigation of the spinup energetics.

The available enthalpy reference state is defined to be a state at which parcels reach equilibrium with the surroundings and no further work can be done. Marquet (1991) suggested an isothermal reference state at constant pressure. Recognizing that the spinup domain encompasses much of the subcloud layer and comprises parcels that rise in convection, the reference state is chosen to be at the initial tropopause with a reference temperature of −70°C and a reference pressure of 135 hPa. The

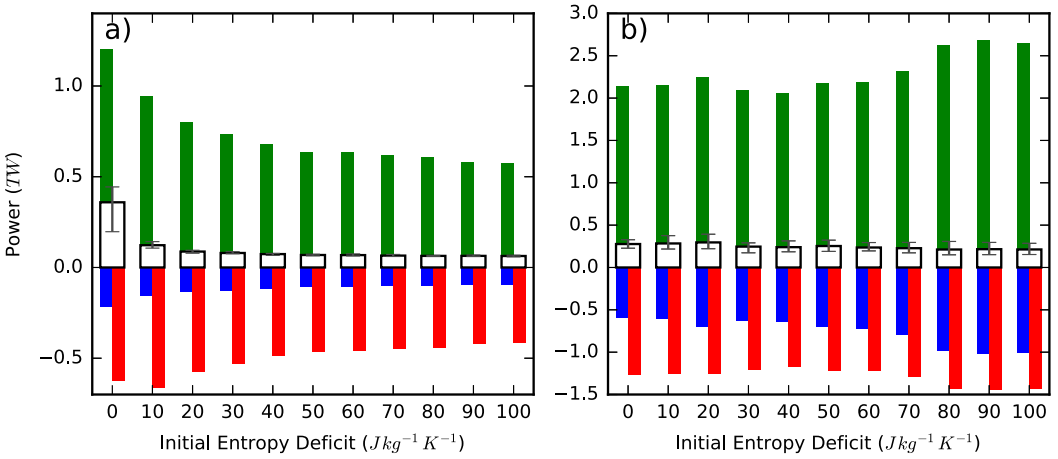

FIG. 13. Ensemble-mean IHKE budget for each experimental set averaged over (a) the period through t_1 and (b) from t_1 to t_2. The green bars give the generation of horizontal kinetic energy due to flow down the radial pressure gradient, the blue bars give the net advective flux of kinetic energy through the spinup domain, and the red bars give the destruction of kinetic energy due to turbulent fluxes. The white (gray) bars give the mean (10th–90th percentiles) rate of change of IHKE. Note the change in vertical scale between (a) and (b).

reference state is also assumed to be saturated. This choice represents an approximate equilibrium level for parcels that rise undiluted. In actuality, the reference state may evolve in both space and time and consists of intermediate states between the cloud base and tropopause. A reference temperature and pressure specified at the tropopause thus represents an upper bound on available enthalpy, and we define it to be the potential available enthalpy. The potential available enthalpy within the spinup domain may not be realized if there is diffusion of water vapor between parcels aloft (Pauluis 2007), analogous to the surface-based convective available potential energy not being fully realized if a parcel entrains dry air from the environment above the surface.

The potential available enthalpy a_p is defined as

$$a_p = h - h_r - T_r(s - s_r), \tag{9}$$

where h is the moist enthalpy and T is the temperature. Any variable with the subscript of r refers to the reference state. There are normally additional terms involving the chemical potentials of water vapor and liquid water in the

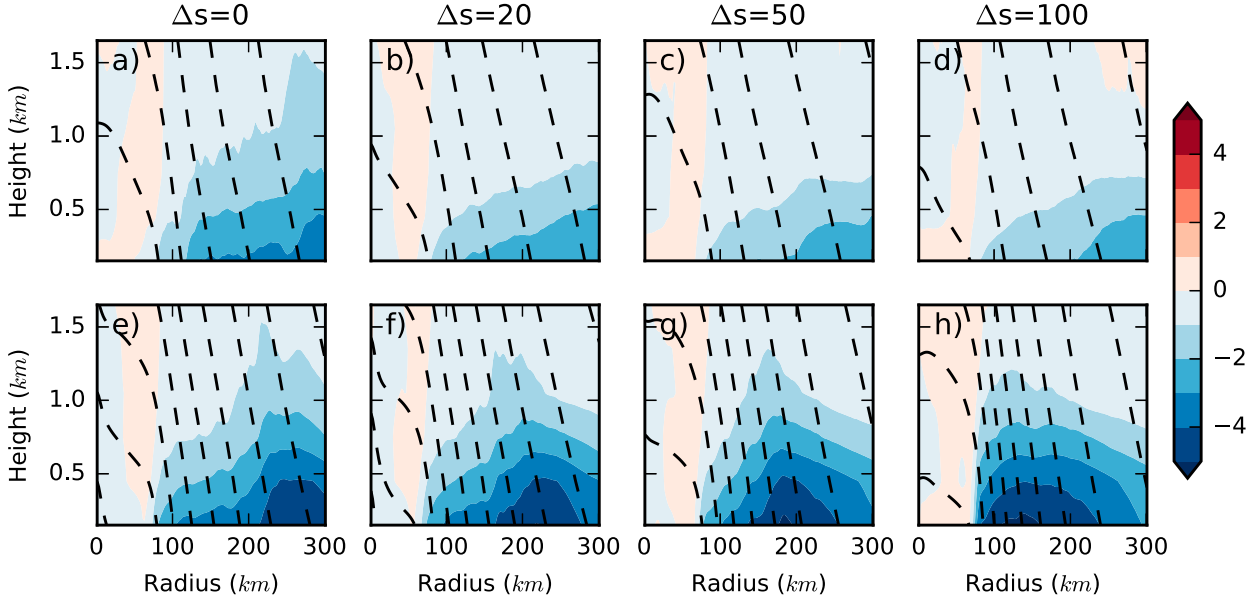

FIG. 14. Ensemble-mean radial wind (shading; m s^{-1}) and horizontal pressure perturbations (dashed contours, every 1 hPa) averaged over (a)–(d) the period through t_1, and (e)–(h) from t_1 to t_2 for (left–right) initial Δs = 0, 20, 50, and 100 J kg^{-1} K^{-1}.

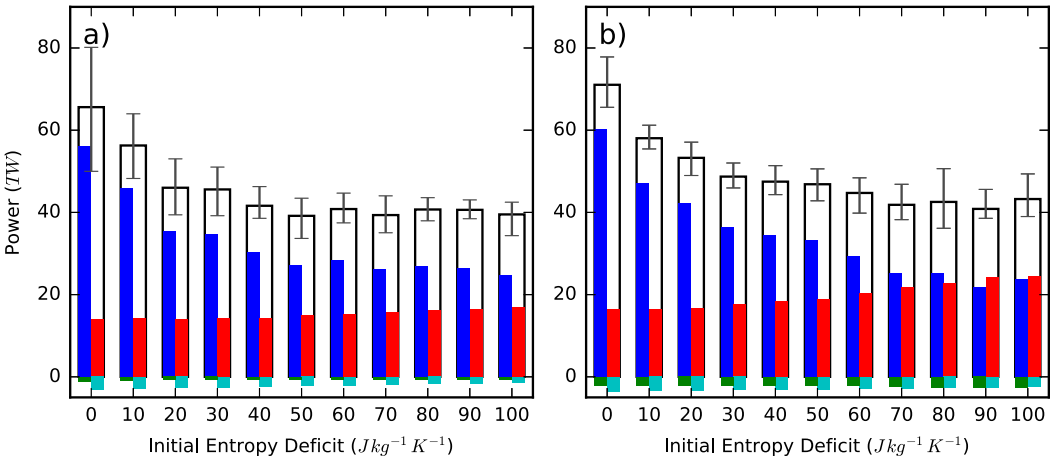

FIG. 15. Ensemble-mean integrated potential available enthalpy budget for each experimental set averaged over (a) the period through t_1 and (b) from t_1 to t_2. The green bars give the loss of potential available enthalpy due to flow down the radial pressure gradient, the blue bars give the net advective flux of potential available enthalpy through the spinup domain, the red bars give the source of potential available enthalpy due to turbulent fluxes, and the cyan bars give the loss of potential available enthalpy due to adiabatic expansion and radiation. The white (gray) bars give the mean (10th–90th percentiles) rate of change of integrated potential available enthalpy.

reference state (Marquet 1993), but these are both neglected. Since the specific heat of liquid water is neglected in favor of an inflated value of the latent heat of vaporization in ASPECH, the chemical potential of liquid water is also neglected for consistency. The choice of a saturated reference state requires the chemical potentials of water vapor and liquid water to be equal, so the chemical potential of water vapor is neglected as well.

The first law of thermodynamics may be expressed as

$$\frac{dh}{dt} = T\frac{ds}{dt} + \alpha\frac{dp}{dt}, \tag{10}$$

where α is the specific volume and p is the pressure. Taking the total derivative of (9), substituting in (10), and converting dp/dt to $d\pi/dt$,

$$\frac{da_p}{dt} = (T - T_r)\frac{ds}{dt} + c_{\mathrm{pd}}\theta_\rho\frac{\partial\pi}{\partial t} + c_{\mathrm{pd}}\theta_\rho\mathbf{u}\cdot\nabla\pi. \tag{11}$$

The first term on the rhs of (11) represents sources of potential available enthalpy due to sources of entropy like surface fluxes and radiation, the second term represents changes due to adiabatic expansion, and the third term represents the conversion of potential available enthalpy to kinetic energy, as seen earlier.

Using the moist entropy equation from ASPECH (TE12),

$$\frac{ds}{dt} = \frac{c_{\mathrm{pd}}\pi}{T}R + D_s, \tag{12}$$

(11) becomes

$$\frac{da_p}{dt} = \frac{T - T_r}{T}c_{\mathrm{pd}}\pi R + (T - T_r)D_s + c_{\mathrm{pd}}\theta_\rho\frac{\partial\pi}{\partial t} + c_{\mathrm{pd}}\theta_\rho\mathbf{u}\cdot\nabla\pi, \tag{13}$$

where R is the radiative heating rate and D_s is turbulent sources of moist entropy.

Defining $A_p = \rho_d a_p$, using conservation of mass, and integrating over the spinup domain yields an integrated form of the potential available enthalpy equation:

$$\frac{\partial}{\partial t}\int_V A_p = -\int_S \mathbf{u}A_p\cdot\mathbf{n} + \int_V \frac{T - T_r}{T}c_{\mathrm{pd}}\rho_d\pi R + \int_V (T - T_r)\rho_d D_s + \int_V c_{\mathrm{pd}}\rho_d\theta_\rho\frac{\partial\pi}{\partial t} + \int_V c_{\mathrm{pd}}\rho_d\theta_\rho\mathbf{u}\cdot\nabla\pi. \tag{14}$$

The terms in (14) compose the left side of Fig. 12. The final term includes both conversions to horizontal and vertical kinetic energy. The latter can be relatively large, but the work performed yields little actual vertical kinetic energy because almost all the work is used by parcels expanding against the environment, leaving nonhydrostatic accelerations to produce vertical kinetic energy. Since the vertical component of the kinetic energy is negligible compared to the horizontal component in the spinup domain, the vertical component of the last term in (14) is not considered in this study.

Figure 15 shows the ensemble-mean potential available enthalpy budget for each experimental set. In comparison with the horizontal kinetic energy budget, the dominant

components are one to two orders of magnitude larger. In fact, the conversion between potential available enthalpy to horizontal kinetic energy (green bars) is barely discernible in Fig. 15. While the conversion term is small compared to the total reservoir of potential available enthalpy, a greater generation rate of potential available enthalpy suggests the potential for parcels in the spinup domain to perform more work to spin up the vortex.

Through t_1, the ensemble-mean rate of increase of potential available enthalpy is about 65 TW for the $\Delta s = 0\,\mathrm{J\,kg^{-1}\,K^{-1}}$ set, decreases monotonically as the initial entropy deficit increases to $50\,\mathrm{J\,kg^{-1}\,K^{-1}}$, and is around 40 TW for $\Delta s \geq 50\,\mathrm{J\,kg^{-1}\,K^{-1}}$ (Fig. 15a). Most of this trend is due to advective fluxes of potential available enthalpy through the sides of the spinup domain. Positive values of the net advective flux indicate greater radial import compared to vertical export of potential available enthalpy, with the imbalance increasing as the initial entropy deficit decreases below $50\,\mathrm{J\,kg^{-1}\,K^{-1}}$. The import of potential available enthalpy is larger than the local source due to surface fluxes. This result is similar to the findings of Fritz and Wang (2014), who showed the inward flux of water vapor exceeded local evaporation in a high-resolution simulation of a developing tropical disturbance. The stronger and deeper radial inflow at 300 km in the lower initial entropy deficit experiments results in a larger radial import of potential available enthalpy into the spinup domain.

Between t_1 and t_2, the same pattern in the rate of increase of potential available enthalpy as a function of the initial entropy deficit persists; however, there are some important differences in the components compared to the period prior to t_1. The source due to net advective fluxes increases for the lower initial entropy deficit experiments, as the secondary circulation increases in strength and the enthalpy within the radial inflow layer remains high. In contrast, the source due to net advective fluxes for the higher initial entropy deficit experiments decreases. The increasing radial inflow is negated by dry, low-enthalpy air entering the inflow layer (Figs. 5h and 5l). The opposite trend is observed in the surface flux component. The $\Delta s = 90$ and $100\,\mathrm{J\,kg^{-1}\,K^{-1}}$ sets have the largest increase in this component, which is a consequence of a larger air–sea disequilibrium between the sea surface saturation enthalpy and the near-surface enthalpy (not shown). As a result, the sources of potential available enthalpy due to net advective fluxes into the spinup domain and turbulent surface fluxes within the spinup domain are nearly equal. Despite the partial compensation of increasing surface fluxes, the decrease in the net advective flux of potential available enthalpy as the initial entropy deficit increases still dominates the overall trend.

In summary, the results indicate that the initial entropy deficit plays a role in the evolution of the energetics. As the initial entropy deficit increases, there is less total generation of potential available enthalpy. The conversion from potential available enthalpy to horizontal kinetic energy is also generally reduced with increasing initial entropy deficit, but only for the period before t_1. Between t_1 and t_2, the larger initial entropy deficit experiments become more efficient by increasing the conversion of potential available enthalpy to horizontal kinetic energy at smaller radii, tied to the small annulus of deep convection. The rate of horizontal kinetic energy generation tends to be similar across all experiments between t_1 and t_2.

6. Sensitivity to spinup domain

The different structural evolution of the low-level vortex across the experimental sets indicates possible sensitivity to the specification of the spinup domain. The specification will always be arbitrary to some degree, but the domain may be chosen a posteriori based on examination of the low-level vortex structure and convection. The important aspect is consistency: that is, the IHKE, spinup times, and other diagnostics should all be calculated over the same domain. An exhaustive evaluation of the sensitivity of the individual components of the angular momentum, kinetic energy, and potential available enthalpy diagnostics is beyond the scope of this study. Instead, we will assess whether the choice of domain changes the basic nature of the spinup time sensitivity to the initial entropy deficit.

The IHKE, spinup time, and average vertical mass flux are calculated as before, but for four domains with an outer radius at 150 or 300 km and a top at 1.5 or 3.0 km. Recall the original domain has an outer radius of 300 km and a top of 1.5 km. Figure 16 shows the ensemble-mean t_1 as a function of the initial entropy deficit for the four domains. The sublinear relationship appears to be robust across the domains such that the greatest sensitivity of spinup time occurs for low initial entropy deficits. Next, the average vertical mass flux for each domain is used to calculate τ_1. Figure 17 shows a comparison between t_1 and τ_1. The spinup time in each domain has a scaling near to that of theoretical expectations, indicating that the theoretical time scale is robust to choice of a reasonable domain that captures the evolution of the structure and intensity of the low-level vortex. Similar results are obtained for t_2 and τ_2 (not shown).

7. Conclusions

The ASPECH model is used to study the sensitivity of tropical cyclone spinup time to the initial entropy deficit.

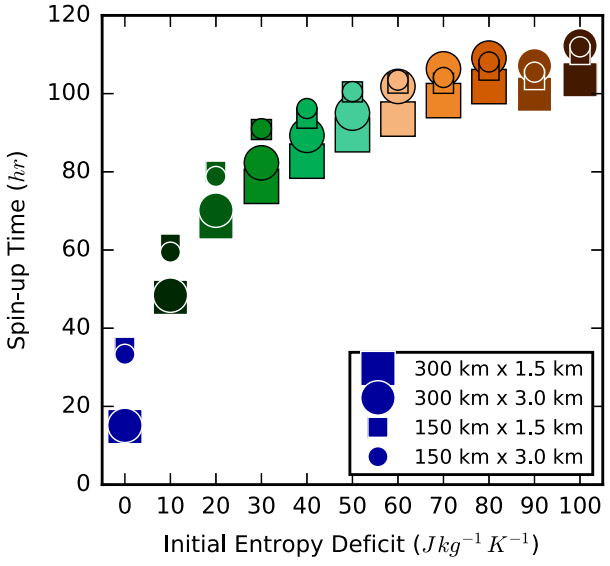

FIG. 16. Ensemble-mean t_1 as a function of the initial entropy deficit for four different spinup domains. Different symbols correspond to different domains (radius × height).

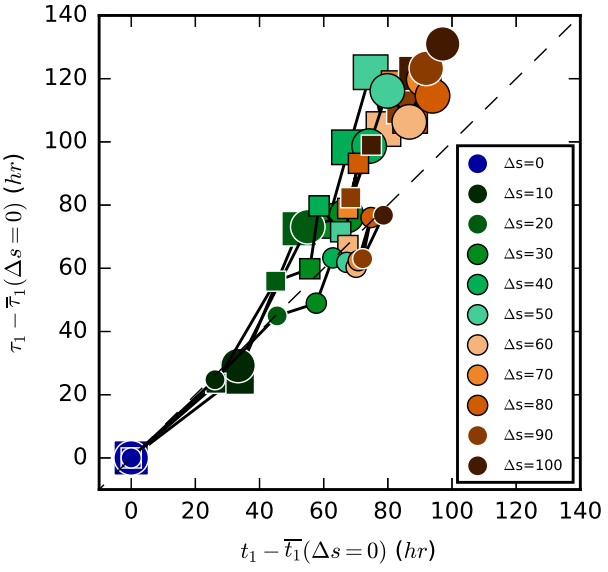

FIG. 17. Experimental spinup time t_1 vs the theoretical spinup time scale τ_1 for four different spinup domains. The symbols used to denote the domains are as in Fig. 16. The dashed line is the one-to-one line. The times are shifted by the mean values for the $\Delta s = 0\,\mathrm{J\,kg^{-1}\,K^{-1}}$ set for each respective domain.

Spinup times are measured by the time it takes the low-level vortex to exceed chosen thresholds of the integrated horizontal kinetic energy. Increasing the entropy deficit results in a longer spinup time, but the relationship is nonlinear. The greatest sensitivity in spinup time is for initial entropy deficits between 0 and $40\,\mathrm{J\,kg^{-1}\,K^{-1}}$. This range encompasses typical values in the tropical free troposphere and may indicate why tropospheric moisture is a statistically significant parameter in empirical genesis indices (DeMaria et al. 2001; Camargo et al. 2007; Emanuel 2010; Tippett et al. 2011). Increasing the entropy deficit also results in a greater range in spinup times, as the stochastic effects of convection on spinup accumulate over a longer period of time.

In reality, there is vertical structure, horizontal inhomogeneity, and time dependence in environmental entropy deficit profiles in the tropics. Storm-relative flow associated with environmental vertical wind shear may inhibit convection from moistening the troposphere and prevent spinup altogether if the entropy deficit remains high. There are many degrees of freedom that make studying spinup time in observations a challenge. Nonetheless, convection is fundamentally sensitive to the tropospheric moisture profile.

The initial entropy deficit affects the evolution of the convection and mass flux. The vertical mass flux profiles suggest simulations with higher entropy deficits have a greater proportion of cumulus congestus during spinup, presumably as convection entrains drier environmental air and destroys buoyancy. The net effect of increasing the entropy deficit is to decrease the vertical mass flux during the spinup period. The Emanuel (1989) scaling depends inversely on the average vertical mass flux through the spinup domain, and the axisymmetric spinup time in the model fits the theoretical scaling well. Hence, understanding processes that control the vertical mass flux is critical for understanding the axisymmetric spinup time.

The vertical mass flux is a component of the secondary circulation, which is structurally sensitive to the initial entropy deficit. A larger initial entropy deficit is associated with delayed development of a tropospheric-deep secondary circulation that also has a radial inflow layer that is weaker and more shallow. The result is a lower influx of angular momentum over a longer period of time. Additionally, there is less import of potential available enthalpy into the spinup domain and a reduction in the conversion from potential available enthalpy to horizontal kinetic energy because of a reduction in the flow down the radial pressure gradient. The angular momentum and energetic points of view are consistent and complement one another.

The potential available enthalpy framework is attractive because of its simplicity in ASPECH but is limited by the choice of a constant reference state. A reference state that varies in space and time may be more realistic but may result in budgets that are

onerous to compute. It is likely that the actual available enthalpy decreases with increasing initial entropy deficit because there are more parcels that have reference states at temperatures higher than the tropopause cold point as a result of entrainment of drier air. A follow-on study will more carefully examine the potential roles of entrainment, either laterally into convection or vertically through Ekman suction or turbulent mixing into the radial inflow layer, during spinup.

The development of tropical cyclone structure is different between the lower and higher entropy deficit experiments because of the width of the envelope of deep convection. The lower entropy deficit experiments have a wider envelope and tend to spin up the vortex more broadly, whereas the higher entropy deficit experiments have a narrower envelope and tend to spin up the vortex more strongly at the nascent radius of maximum wind. Therefore, it appears the initial entropy deficit may play a role in the flavor of spinup, which has implications on the eventual structure of the tropical cyclone, such as its size.

One major question is whether the spinup time scaling applies in a three-dimensional framework. Two-dimensional convection clearly lacks the rich spectrum of asymmetric convection present in tropical disturbances and cyclones (e.g., Houze 2010). Still, we hypothesize that the aggregate effect of three-dimensional convection through the area-averaged mass flux calculated in a similar manner as in these experiments may be important for the system-scale spinup of tropical cyclones (Hendricks et al. 2004). The idealized framework and experimental results with ASPECH allow for a set of hypotheses to test in idealized three-dimensional experiments to investigate whether the axisymmetric results hold. One can also add additional layers of complexity, such as ice microphysics and the role of melting in downdrafts. Such a study should be conducted using an ensemble framework and will be the subject of future work.

Acknowledgments. Three anonymous reviewers helped improve the manuscript. Rosimar Rios-Berrios and Joshua Alland were funded by the National Science Foundation Graduate Research Fellowship Grant DGE 1060277. Rosimar Rios-Berrios was also supported by the NCAR Significant Opportunities in Atmospheric Research and Science (SOARS) program.

REFERENCES

Bannon, P. R., 2004: Lagrangian available energetics and parcel instabilities. *J. Atmos. Sci.*, **61**, 1754–1767, doi:10.1175/1520-0469(2004)061<1754:LAEAPI>2.0.CO;2.

——, 2005: Eulerian available energetics in moist atmospheres. *J. Atmos. Sci.*, **62**, 4238–4252, doi:10.1175/JAS3516.1.

Bister, M., and K. A. Emanuel, 1997: The genesis of Hurricane Guillermo: TEXMEX analyses and a modeling study. *Mon. Wea. Rev.*, **125**, 2662–2682, doi:10.1175/1520-0493(1997)125<2662:TGOHGT>2.0.CO;2.

Black, P. G., and Coauthors, 2007: Air–sea exchange in hurricanes: Synthesis of observations from the Coupled Boundary Layer Air–Sea Transfer experiment. *Bull. Amer. Meteor. Soc.*, **88**, 357–374, doi:10.1175/BAMS-88-3-357.

Bolton, D., 1980: The computation of equivalent potential temperature. *Mon. Wea. Rev.*, **108**, 1046–1053, doi:10.1175/1520-0493(1980)108<1046:TCOEPT>2.0.CO;2.

Brown, R. G., and C. Zhang, 1997: Variability of midtropospheric moisture and its effect on cloud-top height distribution during TOGA COARE. *J. Atmos. Sci.*, **54**, 2760–2774, doi:10.1175/1520-0469(1997)054<2760:VOMMAI>2.0.CO;2.

Bryan, G. H., 2008: On the computation of pseudoadiabatic entropy and equivalent potential temperature. *Mon. Wea. Rev.*, **136**, 5239–5245, doi:10.1175/2008MWR2593.1.

——, and R. Rotunno, 2009: The maximum intensity of tropical cyclones in axisymmetric numerical model simulations. *Mon. Wea. Rev.*, **137**, 1770–1789, doi:10.1175/2008MWR2709.1.

Camargo, S. J., K. A. Emanuel, and A. H. Sobel, 2007: Use of a genesis potential index to diagnose ENSO effects on tropical cyclone genesis. *J. Climate*, **20**, 4819–4834, doi:10.1175/JCLI4282.1.

Davis, C. A., and D. A. Ahijevych, 2012: Mesoscale structural evolution of three tropical weather systems observed during PREDICT. *J. Atmos. Sci.*, **69**, 1284–1305, doi:10.1175/JAS-D-11-0225.1.

DeMaria, M., J. A. Knaff, and B. H. Connell, 2001: A tropical cyclone genesis parameter for the tropical Atlantic. *Wea. Forecasting*, **16**, 219–233, doi:10.1175/1520-0434(2001)016<0219:ATCGPF>2.0.CO;2.

Donelan, M. A., B. K. Haus, N. Reul, W. J. Plant, M. Stiassnie, H. C. Graber, O. B. Brown, and E. S. Saltzman, 2004: On the limiting aerodynamic roughness of the ocean in very strong winds. *Geophys. Res. Lett.*, **31**, L18306, doi:10.1029/2004GL019460.

Dunion, J. P., 2011: Rewriting the climatology of the tropical North Atlantic and Caribbean Sea atmosphere. *J. Climate*, **24**, 893–908, doi:10.1175/2010JCLI3496.1.

Dunkerton, T. J., M. T. Montgomery, and Z. Wang, 2009: Tropical cyclogenesis in a tropical wave critical layer: Easterly waves. *Atmos. Chem. Phys.*, **9**, 5587–5646, doi:10.5194/acp-9-5587-2009.

Emanuel, K. A., 1989: The finite-amplitude nature of tropical cyclogenesis. *J. Atmos. Sci.*, **46**, 3431–3456, doi:10.1175/1520-0469(1989)046<3431:TFANOT>2.0.CO;2.

——, 1995: The behavior of a simple hurricane model using a convective scheme based on subcloud-layer entropy equilibrium. *J. Atmos. Sci.*, **52**, 3960–3968, doi:10.1175/1520-0469(1995)052<3960:TBOASH>2.0.CO;2.

——, 2010: Tropical cyclone activity downscaled from NOAA-CIRES reanalysis, 1908–1958. *J. Adv. Model. Earth Syst.*, **2** (1), doi:10.3894/JAMES.2010.2.1.

——, R. Sundararajan, and J. Williams, 2008: Hurricanes and global warming: Results from downscaling IPCC AR4 simulations. *Bull. Amer. Meteor. Soc.*, **89**, 347–367, doi:10.1175/BAMS-89-3-347.

Fairall, C. W., E. F. Bradley, D. P. Rogers, J. B. Edson, and G. S. Young, 1996: Bulk parameterization of air–sea fluxes for Tropical Ocean–Global Atmosphere Coupled–Ocean Atmosphere Response Experiment. *J. Geophys. Res.*, **101**, 3747–3764, doi:10.1029/95JC03205.

Fritz, C., and Z. Wang, 2014: Water vapor budget in a developing tropical cyclone and its implication for tropical cyclone formation. *J. Atmos. Sci.*, **71**, 4321–4332, doi:10.1175/JAS-D-13-0378.1.

Gray, W. M., 1979: Hurricanes: Their formation, structure and likely role in the tropical circulation. *Meteorology over the Tropical Oceans*, D. B. Shaw, Ed., Royal Meteorological Society, 155–218.

Haus, B. K., D. Jeong, M. A. Donelan, J. A. Zhang, and I. Savelyev, 2010: Relative rates of sea–air heat transfer and frictional drag in very high winds. *Geophys. Res. Lett.*, **37**, L07802, doi:10.1029/2009GL042206.

Hendricks, E. A., M. T. Montgomery, and C. A. Davis, 2004: The role of vertical hot towers in the formation of Tropical Cyclone Diana (1984). *J. Atmos. Sci.*, **61**, 1209–1232, doi:10.1175/1520-0469(2004)061<1209:TROVHT>2.0.CO;2.

Hill, K. A., and G. M. Lackmann, 2009: Influence of environmental humidity on tropical cyclone size. *Mon. Wea. Rev.*, **137**, 3294–3315, doi:10.1175/2009MWR2679.1.

Houze, R. A., 2010: Clouds in tropical cyclones. *Mon. Wea. Rev.*, **138**, 293–344, doi:10.1175/2009MWR2989.1.

James, R. P., and P. M. Markowski, 2010: A numerical investigation of the effects of dry air aloft on deep convection. *Mon. Wea. Rev.*, **138**, 140–161, doi:10.1175/2009MWR3018.1.

Kessler, E., 1969: *On the Distribution and Continuity of Water Substance in Atmospheric Circulations*. *Meteor. Monogr.*, No. 10, Amer. Meteor. Soc., 88 pp.

Knaff, J. A., C. R. Sampson, P. J. Fitzpatrick, Y. Jin, and C. M. Hill, 2011: Simple diagnosis of tropical cyclone structure via pressure gradients. *Wea. Forecasting*, **26**, 1020–1031, doi:10.1175/WAF-D-11-00013.1.

Komaromi, W. A., 2013: An investigation of composite dropsonde profiles for developing and nondeveloping tropical waves during the 2010 PREDICT field campaign. *J. Atmos. Sci.*, **70**, 542–558, doi:10.1175/JAS-D-12-052.1.

Lorenz, E. N., 1955: Available potential energy and the maintenance of the general circulation. *Tellus*, **7A**, 157–167, doi:10.1111/j.2153-3490.1955.tb01148.x.

——, 1978: Available energy and the maintenance of a moist circulation. *Tellus*, **30A**, 15–31, doi:10.1111/j.2153-3490.1978.tb00815.x.

Marquet, P., 1991: On the concept of exergy and available enthalpy: Application to atmospheric energetics. *Quart. J. Roy. Meteor. Soc.*, **117**, 449–475, doi:10.1002/qj.49711749903.

——, 1993: Exergy in meteorology: Definition and properties of moist available enthalpy. *Quart. J. Roy. Meteor. Soc.*, **119**, 567–590, doi:10.1002/qj.49711951112.

Musgrave, K. D., R. K. Taft, J. L. Vigh, B. D. McNoldy, and W. H. Schubert, 2012: Time evolution of the intensity and size of tropical cyclones. *J. Adv. Model. Earth Syst.*, **4**, M08001, doi:10.1029/2011MS000104.

Nicholls, M. E., and M. T. Montgomery, 2013: An examination of two pathways to tropical cyclogenesis occurring in idealized simulations with a cloud-resolving numerical model. *Atmos. Chem. Phys.*, **13**, 5999–6022, doi:10.5194/acp-13-5999-2013.

Nolan, D. S., 2007: What is the trigger for tropical cyclogenesis? *Aust. Meteor. Mag.*, **56**, 241–266.

Pauluis, O., 2007: Sources and sinks of available potential energy in a moist atmosphere. *J. Atmos. Sci.*, **64**, 2627–2641, doi:10.1175/JAS3937.1.

Rappin, E. D., D. S. Nolan, and K. A. Emanuel, 2010: Thermodynamic control of tropical cyclogenesis in environments of radiative-convective equilibrium with shear. *Quart. J. Roy. Meteor. Soc.*, **136**, 1954–1971, doi:10.1002/qj.706.

Raymond, D. J., 1995: Regulation of moist convection over the west Pacific warm pool. *J. Atmos. Sci.*, **52**, 3945–3959, doi:10.1175/1520-0469(1995)052<3945:ROMCOT>2.0.CO;2.

——, 2013: Sources and sinks of entropy in the atmosphere. *J. Adv. Model. Earth Syst.*, **5**, 755–763, doi:10.1002/jame.20050.

——, C. Lopez-Carrillo, and L. L. Cavazos, 1998: Case-studies of developing east Pacific easterly waves. *Quart. J. Roy. Meteor. Soc.*, **124**, 2005–2034, doi:10.1002/qj.49712455011.

——, S. L. Sessions, and Z. Fuchs, 2007: A theory for the spinup of tropical depressions. *Quart. J. Roy. Meteor. Soc.*, **133**, 1743–1754, doi:10.1002/qj.125.

——, ——, and C. Lopez Carrillo, 2011: Thermodynamics of tropical cyclogenesis in the northwest Pacific. *J. Geophys. Res.*, **116**, D18101, doi:10.1029/2011JD015624.

Rogers, R., P. Reasor, and S. Lorsolo, 2013: Airborne Doppler observations of the inner-core structural differences between intensifying and steady-state tropical cyclones. *Mon. Wea. Rev.*, **141**, 2970–2991, doi:10.1175/MWR-D-12-00357.1.

Rotunno, R., and K. A. Emanuel, 1987: An air–sea interaction theory for tropical cyclones. Part II: Evolutionary study using a nonhydrostatic axisymmetric numerical model. *J. Atmos. Sci.*, **44**, 542–561, doi:10.1175/1520-0469(1987)044<0542:AAITFT>2.0.CO;2.

Shapiro, L. J., and H. E. Willoughby, 1982: The response of balanced hurricanes to local sources of heat and momentum. *J. Atmos. Sci.*, **39**, 378–394, doi:10.1175/1520-0469(1982)039<0378:TROBHT>2.0.CO;2.

Smith, R. K., 2000: The role of cumulus convection in hurricanes and its representation in hurricane models. *Rev. Geophys.*, **38**, 465–489, doi:10.1029/1999RG000080.

——, 2006: Accurate determination of a balanced axisymmetric vortex in a compressible atmosphere. *Tellus*, **58A**, 98–103, doi:10.1111/j.1600-0870.2006.00149.x.

——, and M. T. Montgomery, 2012: Observations of the convective environment in developing and non-developing tropical disturbances. *Quart. J. Roy. Meteor. Soc.*, **138**, 1721–1739, doi:10.1002/qj.1910.

——, ——, and N. Van Sang, 2009: Tropical cyclone spin-up revisited. *Quart. J. Roy. Meteor. Soc.*, **135**, 1321–1335, doi:10.1002/qj.428.

Tang, B., and K. Emanuel, 2012a: Sensitivity of tropical cyclone intensity to ventilation in an axisymmetric model. *J. Atmos. Sci.*, **69**, 2394–2413, doi:10.1175/JAS-D-11-0232.1.

——, and ——, 2012b: A ventilation index for tropical cyclones. *Bull. Amer. Meteor. Soc.*, **93**, 1901–1912, doi:10.1175/BAMS-D-11-00165.1.

Thayer-Calder, K., and D. Randall, 2015: A numerical investigation of boundary layer quasi-equilibrium. *Geophys. Res. Lett.*, **42**, 550–556, doi:10.1002/2014GL062649.

Tippett, M. K., S. J. Camargo, and A. H. Sobel, 2011: A Poisson regression index for tropical cyclone genesis and the role of large-scale vorticity in genesis. *J. Climate*, **24**, 2335–2357, doi:10.1175/2010JCLI3811.1.

Van Sang, N., R. K. Smith, and M. T. Montgomery, 2008: Tropical-cyclone intensification and predictability in three dimensions. *Quart. J. Roy. Meteor. Soc.*, **134**, 563–582, doi:10.1002/qj.235.

Vigh, J. L., and W. H. Schubert, 2009: Rapid development of the tropical cyclone warm core. *J. Atmos. Sci.*, **66**, 3335–3350, doi:10.1175/2009JAS3092.1.

Wang, Y., 2009: How do outer spiral rainbands affect tropical cyclone structure and intensity? *J. Atmos. Sci.*, **66**, 1250–1273, doi:10.1175/2008JAS2737.1.

Wang, Z., 2012: Thermodynamic aspects of tropical cyclone formation. *J. Atmos. Sci.*, **69**, 2433–2451, doi:10.1175/JAS-D-11-0298.1.

——, 2014: Role of cumulus congestus in tropical cyclone formation in a high-resolution numerical model simulation. *J. Atmos. Sci.*, **71**, 1681–1700, doi:10.1175/JAS-D-13-0257.1.

Ying, Y., and Q. Zhang, 2012: A modeling study on tropical cyclone structural changes in response to ambient moisture variations. *J. Meteor. Soc. Japan*, **90**, 755–770, doi:10.2151/jmsj.2012-512.

Zawislak, J., and E. J. Zipser, 2014: Analysis of the thermodynamic properties of developing and nondeveloping tropical disturbances using a comprehensive dropsonde dataset. *Mon. Wea. Rev.*, **142**, 1250–1264, doi:10.1175/MWR-D-13-00253.1.

Zhang, F., and J. A. Sippel, 2009: Effects of moist convection on hurricane predictability. *J. Atmos. Sci.*, **66**, 1944–1961, doi:10.1175/2009JAS2824.1.